

A Self-Supervised, Differentiable Kalman Filter for Uncertainty-Aware Visual-Inertial Odometry

Brandon Wagstaff¹, Emmett Wise¹, and Jonathan Kelly^{1†}

Abstract—Traditionally, visual-inertial-odometry (VIO) systems rely on filtering or optimization-based frameworks for robot egomotion estimation. While these methods are accurate under nominal conditions, they are prone to failure in degraded environments, where illumination changes, fast camera motion, or textureless scenes are present. Learning-based systems have the potential to outperform classical implementations in degraded environments, but are, currently, less accurate than classical methods in nominal settings. A third class, of *hybrid* systems, attempts to leverage the advantages of both systems.

Herein, we introduce a framework for training a hybrid VIO system. Our approach uses a differentiable Kalman filter with an IMU-based process model and a robust, neural network-based relative pose measurement model. By utilizing the data-efficiency of self-supervised learning, we show that our system significantly outperforms a similar, supervised system, while enabling online retraining. To demonstrate the utility of our approach, we evaluate our system on a visually degraded version of the EuRoC dataset. Notably, we find that, in cases where classical estimators consistently diverge, our estimator does not diverge or suffer from a significant reduction in accuracy. Finally, our system, by properly utilizing the metric information contained in the IMU measurements, is able to recover metric scale, while other self-supervised monocular VIO approaches cannot.

I. INTRODUCTION

Self-localization algorithms that maintain an accurate estimate of a robot’s egomotion or pose (i.e., position, velocity, and orientation) in challenging environments is a fundamental component of modern autonomy. While self-localization algorithms exist in many forms, a common solution is visual-inertial odometry (VIO). VIO fuses camera and inertial measurement unit (IMU) data to estimate a robot’s egomotion [1]; these sensors are inexpensive, lightweight, and enable six degree-of-freedom pose estimation with metric scale. Traditionally, VIO approaches rely on classical filtering or optimization-based back-ends to estimate the local pose change that best explains the relative motion of tracked visual features between frames. However, these heuristic VIO feature trackers are “brittle” in challenging environments (e.g., scenes with motion blur). Recent work has explored data-driven replacements for these brittle classical systems.

In data-driven systems, neural networks are trained via supervised [2]–[4] or self supervised [5], [6] losses to model the complex relationship between the sensor measurements and robot egomotion. While neural networks trained with these loss functions are increasing in popularity and accuracy, they both have major flaws. Neural networks trained using supervised loss functions struggle to generalize beyond the initial training set. The generalization of supervised neural networks improves with the inclusion of more data, but

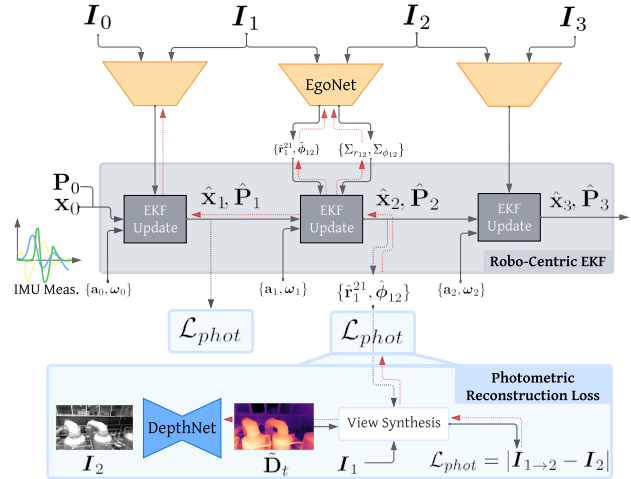


Fig. 1: Overview of our hybrid method that combines an IMU-based process model with a learned relative pose measurement model through a robo-centric extended Kalman filter (EKF). Our self-supervised formulation can train this system end-to-end by minimizing a photometric reconstruction loss. Unlike basic self-supervised VO or VIO systems that directly use the egomotion prediction for view synthesis, we use the *a posteriori* egomotion estimate produced by the EKF, which refines the network output by incorporating inertial measurements.

labelling this data is costly. Consequently, self-supervised loss formulations, which do not require data labelling, are replacing supervised formulations. Despite recent advances [5], [6], self-supervised approaches do not leverage knowledge from the domain of sensor fusion, so network-based approaches provide no notion of uncertainty with their predictions. Further, these approaches do not properly utilize the scale information contained within the IMU measurements, which is fundamental in classical sensor fusion.

Herein, we propose a novel *hybrid* system that leverages the benefits—and mitigates the limitations—of classical and learning-based VIO systems. Our sensor fusion scheme (illustrated in Figure 1) uses a differentiable filter (DF) [7] to incorporate network-based egomotion measurements into our uncertainty-aware state estimate, which additionally relies on an IMU-based process model to propagate the state between camera frames. Our work builds upon that of Li et al. [8], who used supervised pose labels to train an end-to-end system. We relax these training requirements by replacing the supervised loss with a pixel-based reconstruction loss that is fully self-supervised. Notably, our approach is the first self-supervised, monocular method that produces metrically scaled predictions. These predictions are *uncertainty-aware*—we incorporate a learned heteroscedastic uncertainty

model, allowing for principled fusion of the measurements within the filter. Our experiments demonstrate, relative to classical systems, the robustness of our algorithm to visually degraded environments.

II. RELATED WORK

In this section, we separate existing approaches to VIO into three categories: classical, learned, and hybrid, which refer to the amount of (or the lack thereof) machine learning involved in each case.

A. Classical Approaches to VIO

Generally, VIO algorithms are composed of a front-end and a back-end. The front-end detects and tracks features across images. The back-end estimates the 3D locations of tracked features and camera trajectory in a loosely- or tightly-coupled formulation. Loosely coupled methods independently estimate the state with each sensor modality, and combine the estimates in a final stage. Conversely, tightly-coupled methods incorporate each sensor modality in a joint estimation framework. The frameworks minimize the reprojection error between predicted and observed feature locations. The reprojection error is either indirect, in terms of pixel coordinates, or direct, in terms of photometric loss.

Once the sensor coupling is chosen, the reprojection error is minimized using a filter- or optimization-based algorithm. One well-known filter-based algorithm is the multi-state constraint Kalman Filter (MSCKF) [9], but its world-centric formulation is inconsistent [10]. This inconsistency led to robot-centric formulations such as ROVIO [11] and R-VIO [12]. Optimization-based algorithms such as VINS-Mono [13] and OK-VIS [14] optimize over a window of poses, while relying on IMU preintegration [15] to make the IMU factors tractable. Although more computationally intensive, optimization approaches are more accurate than their filter-based counterparts. Herein, we demonstrate how several classical methods (namely VINS-Mono, ROVIO, and R-VIO) are prone to failure in visually degraded scenes.

B. Learning-Based Approaches to VIO

Recent neural network-based visual-inertial fusion schemes [2]–[6] all adopt a similar “feature fusion” scheme, where a neural network maps the raw (visual and inertial) measurements to a 6-DOF egomotion prediction in an end-to-end manner. Internally, the network extracts and combines (e.g., through concatenation of the two feature vectors) sensor-specific features. The resulting multimodal features pass into a final network component that predicts the egomotion. This scheme exists in both supervised [2]–[4] and self-supervised [5], [6] settings. In the self-supervised setting [16], a pixel-based reconstruction loss is minimized to jointly train a depth and egomotion network. The training process leverages the depth and egomotion predictions to project pixels from a nearby source image into a target frame, also known as view synthesis. The pixel-based reconstruction loss is the per-pixel photometric difference between the projected image and an image taken in the

target frame. Since view synthesis generates a more realistic projected image as the depth and egomotion estimates improve, the networks can be trained by minimizing the pixel-based loss.

While end-to-end approaches are effective, they do not utilize the canonical relationship between inertial measurements and robot dynamics. Ignoring this relationship burdens the network with learning well-modelled kinematics and prevents the network from utilizing the metric information in the inertial measurements. To utilize the linear acceleration outputs, the network must learn implicitly to track the robot’s velocity. To remove gravity from the acceleration measurements, the network must also learn to track the global IMU orientation. Finally, the metric information available from inertial measurements cannot be utilized because reconstruction-based losses do not account for scale. Consequently, the depth and egomotion predictions are only accurate up to scale. Herein, our aim is to resolve these issues with our hybrid approach, which, in contrast to the feature-fusion approach, combines visual and inertial information in a probabilistic manner.

C. Hybrid Approaches to VIO

Differentiable filters (DFs) have been proposed as a way to impose prior knowledge into the network structure by combining *perception* (i.e., through a measurement model that maps sensory observations to the state) and *prediction* (i.e., through a process model that determines how the state changes over time) in a Bayesian fashion [7], [17]. Being fully differentiable, DF’s can be trained end-to-end to produce uncertainty-aware measurement and process models that accurately model the noise characteristics that are present. The DF is particularly useful for replacing (brittle) hand-crafted measurement models with networks that directly map high dimensional, nonlinear measurements (e.g., raw images) onto to the state. Application of this hybrid structure in visual applications include camera relocalization [18], object tracking [17], and VIO. Chen et al. [19] use a DF to learn the noise parameters of an EKF-based VIO system. The authors of [20], through a feature fusion scheme, train a visual-inertial measurement model for a Kalman filter with a learned process model. Li et al. [8] present a DF that combines a classical IMU-based process model with a learned relative pose measurement model. Their network was trained end-to-end by minimizing a pose supervision loss. We extend the approach of Li et al. [8] by training the network with a photometric reconstruction loss, which improves the overall system accuracy by leveraging the data efficiency of self-supervised learning. To the best of the authors’ knowledge, we are the first to train a differentiable filter in a fully self-supervised manner.

III. APPROACH

Our hybrid approach to VIO augments the learned depth and egomotion estimation system with a robo-centric EKF back-end. By doing so, the photometric reconstruction loss can be computed with the refined, *a posteriori* egomotion

estimate, rather than the direct network output. This posterior estimate, notably, is a function of the inertial measurements used to propagate the state via the process model. Since the filter structure is fully differentiable, the whole system can be trained end-to-end by minimizing the photometric reconstruction loss.

In Section III-A, we review the notation that is used in this paper. In Section III-B, we discuss the self-supervised depth and egomotion estimation formulation. In Section III-C, we review the robocentric VIO EKF. In Section III-D, we present our end-to-end training scheme that minimizes the self-supervised reconstruction loss.

A. Notation

We begin by defining four reference frames that are used throughout Section III. Let $\mathcal{F}_{\rightarrow i}$, $\mathcal{F}_{\rightarrow c_k}$, $\mathcal{F}_{\rightarrow r_k}$, $\mathcal{F}_{\rightarrow v_\tau}$ represent a static reference frame, the camera reference frame at time k , the robo-centric reference frame at time k , and the IMU reference frame at time τ , respectively. The scalars k and τ are the image and IMU timesteps. Unbolded lower case letters are reserved for scalar quantities. One exception is δ , which denotes the perturbation of the subsequent quantity. Bolded lower case and greek letters represent vector quantities. The vector $\mathbf{g}_a \in \mathbb{R}^3$ is the gravity vector expressed in $\mathcal{F}_{\rightarrow a}$. The vectors $\mathbf{b}_{\omega_k}, \mathbf{b}_{a_k} \in \mathbb{R}^3$ are, respectively, the IMU rotational and acceleration bias at time k . The vectors $\mathbf{r}_a^{ba}, \mathbf{v}_a^{ba}, \boldsymbol{\omega}_a^{ba}, \mathbf{a}_a^{ba} \in \mathbb{R}^3$ are the translation, linear velocity, rotational velocity, and linear acceleration of $\mathcal{F}_{\rightarrow b}$ with respect to $\mathcal{F}_{\rightarrow a}$ expressed in $\mathcal{F}_{\rightarrow a}$. The noise vector of quantity i is represented using $\mathbf{n}_i \approx \mathcal{N}(\mathbf{0}, \sigma_i^2 \mathbf{1})$. Bolded upper case and greek letters represent matrix quantities. We reserve $\mathbf{C}_{ab} \in \text{SO}(3)$ as the rotation matrix that rotates vectors from $\mathcal{F}_{\rightarrow b}$ to $\mathcal{F}_{\rightarrow a}$. The (known) extrinsic transform between $\mathcal{F}_{\rightarrow c}$ and $\mathcal{F}_{\rightarrow r}$ consists of the rotation matrix \mathbf{C}_{rc} and the translation \mathbf{r}_{rc}^{cr} . The vector $\boldsymbol{\phi}_{ab} \in \mathbb{R}^3$ is used to denote the Lie algebra vector of \mathbf{C}_{ab} . Perturbations of the rotation state are given by $\mathbf{C}_{ab} = \bar{\mathbf{C}}_{ab} \exp(\delta \boldsymbol{\phi}_{ab}^\wedge)$, where $(\cdot)^\wedge$ is the nominal rotation matrix. The operator $(\cdot)^\wedge$ is the skew-symmetric operator. $(\tilde{\cdot})$ denotes a learned estimate.

B. Self-Supervised Depth and Egomotion Estimation

We employ a depth network to produce a depth prediction $\tilde{\mathbf{D}}_t$ for a target image \mathbf{I}_t , and an egomotion network to produce an egomotion prediction $\tilde{\mathbf{T}}_{st} \in \text{SE}(3) = \{\tilde{\mathbf{r}}_{c_s c_t}^{c_t c_s}, \tilde{\mathbf{C}}_{c_s c_t} \in \text{SO}(3)\}$ that is an estimate of the 6-DOF pose change between $\mathcal{F}_{\rightarrow c}$ at time t and s . Using these predicted quantities, and the known camera intrinsics \mathbf{K} , we can “reconstruct” each pixel \mathbf{u}' within \mathbf{I}_t by determining its corresponding location, \mathbf{u} , in the nearby source image \mathbf{I}_s using a pinhole camera model π :

$$\mathbf{I}_{s \rightarrow t}(\mathbf{u}') = \mathbf{I}_s(\mathbf{u}), \quad \mathbf{u} = \pi(\tilde{\mathbf{T}}_{st} \pi^{-1}(\mathbf{u}')). \quad (1)$$

The pinhole projection model maps a 3D point $\mathbf{p} = [x \ y \ z]^\top$ to its pixel coordinate \mathbf{u} through $\pi(\mathbf{p}) = \mathbf{K} \frac{1}{z} \mathbf{p}$. Note that in practice, the reconstructed image $\mathbf{I}_{s \rightarrow t}$ is produced using a spatial transformer [21].

After view synthesis, the photometric reconstruction loss can be computed by comparing the reconstructed image with the known target image:

$$\mathcal{L}_{phot}(\mathbf{I}_{s \rightarrow t}, \mathbf{I}_t) = (1 - \alpha) |\mathbf{I}_{s \rightarrow t} - \mathbf{I}_t| + \alpha \mathcal{L}_{SSIM}(\mathbf{I}_{s \rightarrow t}, \mathbf{I}_t), \quad (2)$$

which is a standard combination of the L_1 loss and the structural similarity (SSIM) loss [22]. We use the minimum reconstruction formulation from Godard et al. [23], which, for a given target image, builds \mathcal{L}_{phot} with the minimum per-pixel error values from two adjacent source images:

$$\min_{s \in \{t-1, t+1\}} \mathcal{L}_{phot}(\mathbf{I}_t, \mathbf{I}_{s \rightarrow t}). \quad (3)$$

The depth and egomotion network weights are jointly trained to minimize this reconstruction loss through gradient descent. In addition to \mathcal{L}_{phot} , we employ two auxiliary losses: the depth smoothness [24] \mathcal{L}_{smooth} and the geometric consistency loss $\mathcal{L}_{consist}$ [25]. The automasking method from [23] and the self-discovered mask from [25] are used to remove unreliable pixels.

We train the tightly-coupled networks from Wagstaff et al. [26], as they have been shown to significantly boost egomotion accuracy on challenging indoor datasets. Notably, their egomotion network relies on multiple forward passes to iteratively refine the initial egomotion prediction (refer to [26] for additional details). In Section III-D, we discuss how this network structure is extended to produce uncertainty-aware predictions for incorporating these measurements into the EKF.

C. Robocentric EKF Formulation

Our Robocentric EKF formulation is based on the approach from Li et al. [8]. An in-depth explanation of the formulation can be found in [8], [27].

The set of parameters that we wish to estimate, \mathbf{x} , at the latest IMU measurement, τ , is,

$$\mathbf{x}_\tau = \left[\begin{array}{c|c} \mathbf{C}_{r_k i} & \mathbf{r}_{r_k}^{i r_k} \ \mathbf{g}_{r_k} \\ \mathbf{C}_{r_k v_\tau} & \mathbf{r}_{r_k}^{v_\tau r_k} \ \mathbf{v}_{v_\tau}^{v_\tau i} \ \mathbf{b}_{\omega_k} \ \mathbf{b}_{a_k} \end{array} \right], \quad (4)$$

where the vertical bar separates the inertial states, $\mathbf{x}_{r_k i}$, and the robot states $\mathbf{x}_{r_k v_\tau}$. The error state vector is,

$$\delta \mathbf{x}_\tau = \left[\begin{array}{c|c} \delta \boldsymbol{\phi}_{r_k i}^\top & \delta \mathbf{r}_{r_k}^{i r_k \top} \ \delta \mathbf{g}_{r_k}^\top \\ \delta \boldsymbol{\phi}_{r_k v_\tau}^\top & \delta \mathbf{r}_{r_k}^{v_\tau r_k \top} \ \delta \mathbf{v}_{v_\tau}^{v_\tau i \top} \ \delta \mathbf{b}_{\omega_k}^\top \ \delta \mathbf{b}_{a_k}^\top \end{array} \right]^\top, \quad (5)$$

which contains perturbations of \mathbf{x} .

1) *Process Model and Covariance Propagation*: To determine the error state vector process model, the IMU measurement model and time derivative of the robot state are required. The IMU measurement model is

$$\begin{aligned} \mathbf{a}_m &= \mathbf{a}_{v_\tau}^{v_\tau i} + \mathbf{C}_{v_\tau r_k} \mathbf{g}_{r_k} + \mathbf{b}_{a_\tau} + \mathbf{n}_a, \\ \boldsymbol{\omega}_m &= \boldsymbol{\omega}_{v_\tau}^{v_\tau i} + \mathbf{b}_{\omega_\tau} + \mathbf{n}_\omega. \end{aligned} \quad (6)$$

The time derivative of the robot state set is

$$\dot{\mathbf{x}}_{r_k v_\tau} = \left[\begin{array}{c|c} \mathbf{C}_{r_k v_\tau} \boldsymbol{\omega}_{v_\tau}^{v_\tau i \wedge} & \mathbf{C}_{r_k v_\tau} \mathbf{v}_{v_\tau}^{v_\tau i} \\ \mathbf{a}_{v_\tau}^{v_\tau i} - \boldsymbol{\omega}_{v_\tau}^{v_\tau i \wedge} \mathbf{v}_{v_\tau}^{v_\tau i} & \mathbf{n}_{b_\omega} \ \mathbf{n}_{b_a} \end{array} \right]. \quad (7)$$

By applying perturbations to the state, substituting in Equations 6 and 7, and linearizing the result, the time derivative of the error state vector is

$$\delta \dot{\mathbf{x}}_\tau = \mathbf{F} \delta \mathbf{x}_\tau + \mathbf{G} \mathbf{n}, \quad (8)$$

where $\mathbf{n} = [\mathbf{n}_\omega^\top \quad \mathbf{n}_a^\top \quad \mathbf{n}_{b_\omega}^\top \quad \mathbf{n}_{b_a}^\top]^\top$. \mathbf{G} and \mathbf{F} can be found in [12].

The nominal process model is

$$\check{\mathbf{C}}_{r_k v_{k+1}} = \int_{s \in [t_k, t_{k+1}]} \check{\mathbf{C}}_{r_k v_s} (\boldsymbol{\omega}_m - \check{\mathbf{b}}_{\omega_s})^\wedge ds, \quad (9)$$

$$\check{\mathbf{v}}_{r_k}^{v_{k+1}i} = \hat{\mathbf{v}}_{r_k}^{v_k i} - \check{\mathbf{g}}_{r_k} \Delta t + \int_{s \in [t_k, t_{k+1}]} \check{\mathbf{C}}_{r_k v_s} (\mathbf{a}_m - \check{\mathbf{b}}_{a_s}) ds, \quad (10)$$

$$\check{\mathbf{r}}_{r_k}^{v_{k+1}r_k} = \hat{\mathbf{v}}_{r_k}^{v_k i} - \frac{1}{2} \check{\mathbf{g}}_{r_k} \Delta t^2 + \iint_{s \in [t_k, t_{k+1}]} \check{\mathbf{C}}_{r_k v_s} (\mathbf{a}_m - \check{\mathbf{b}}_{a_s}) ds^2. \quad (11)$$

Discrete integration of the process model is performed using Euler's method.

The transition matrix for the error state vector is

$$\Phi_{\tau+1\tau} = \exp \left(\int_{t_\tau}^{t_{\tau+1}} \mathbf{F}(s) ds \right) \approx \mathbf{1} + \mathbf{F}_\tau \delta t. \quad (12)$$

The predicted state uncertainty is then

$$\mathbf{Q} = \text{diag}(\sigma_\omega^2 \mathbf{1}, \sigma_a^2 \mathbf{1}, \sigma_{b_\omega}^2 \mathbf{1}, \sigma_{b_a}^2 \mathbf{1}), \quad (13)$$

$$\check{\mathbf{P}}_{\tau+1} = \Phi_{\tau+1\tau} \check{\mathbf{P}}_\tau \Phi_{\tau+1\tau}^\top + \mathbf{G} \mathbf{Q} \mathbf{G}^\top \delta t. \quad (14)$$

2) *Measurement Update*: Our measurements are the relative pose changes (egomotion) produced by our network. Unlike current supervised loss formulations, our self-supervised loss requires the egomotion predictions to be camera-centric (i.e., expressed in \mathcal{F}_{c_k}). The measurement residual $\epsilon_{k+1} = [\epsilon_\theta^\top \quad \epsilon_r^\top]^\top$ with covariance \mathbf{R}_k therefore is

$$\begin{bmatrix} \epsilon_\theta \\ \epsilon_r \end{bmatrix} = \begin{bmatrix} \ln(\check{\mathbf{C}}_{c_k c_{k+1}} \mathbf{C}_{c_k c_{k+1}}^\top)^\vee \\ \check{\mathbf{r}}_{c_k}^{c_{k+1}c_k} - \mathbf{r}_{c_k}^{c_{k+1}c_k} \end{bmatrix}, \quad (15)$$

where

$$\mathbf{r}_{c_k}^{c_{k+1}c_k} = \mathbf{C}_{rc}^\top \mathbf{C}_{r_k v_{k+1}} \mathbf{r}_r^{cr} + \mathbf{C}_{rc}^\top (\mathbf{r}_{r_k}^{v_{k+1}r_k} - \mathbf{r}_r^{cr}), \quad (16)$$

$$\mathbf{C}_{c_k c_{k+1}} = \mathbf{C}_{rc}^\top \mathbf{C}_{r_k v_{k+1}} \mathbf{C}_{rc}. \quad (17)$$

The measurement Jacobian $\mathbf{H}_{k+1} = \frac{\partial \epsilon_{k+1}}{\partial \delta \mathbf{x}_{k+1}}$ is found by differentiating Equation (15) with respect to $\delta \mathbf{x}$:

$$\mathbf{H}_{k+1} = \begin{bmatrix} \mathbf{0}_{9 \times 3} & -\mathbf{C}_{rc}^\top \mathbf{J}_\ell(-\check{\phi}_{r_k v_{k+1}}) & \mathbf{0}_{9 \times 3} \\ \mathbf{0}_{9 \times 3} & \mathbf{C}_{rc}^\top \check{\mathbf{C}}_{r_k v_{k+1}} \mathbf{r}_r^{cr \wedge} & -\mathbf{C}_{rc}^\top \mathbf{0}_{9 \times 3} \end{bmatrix}. \quad (18)$$

Note that the derivation for \mathbf{H}_{k+1} uses the Baker-Campbell-Hausdorff (BCH) formula,

$$\ln \left(\exp(\check{\phi}_{c_k c_{k+1}}^\wedge) \exp(\phi_{c_k c_{k+1}}^\wedge)^\top \right)^\vee \approx \check{\phi}_{c_k c_{k+1}} - \phi_{c_k c_{k+1}}, \quad (19)$$

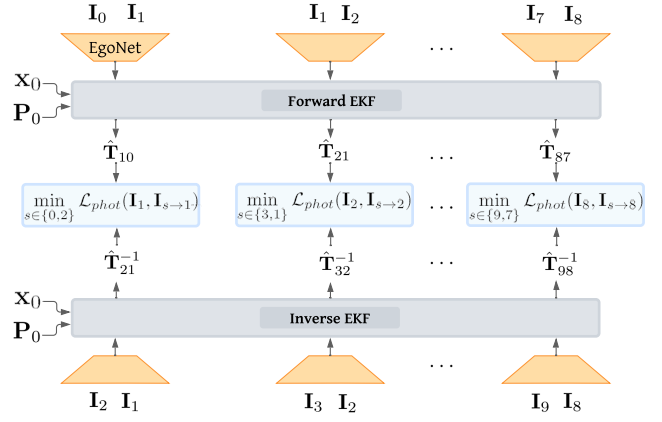


Fig. 2: With the minimum reconstruction loss from [23], two (adjacent) source images are projected into each target frame. We use the egomotion estimates from a forward and inverse EKF to produce these two reconstructions. Samples with N frames can produce $N - 2$ minimum reprojection losses.

which is reasonable for odometry applications. Using the derived equations, the EKF measurement update is

$$\begin{aligned} \mathbf{K}_{k+1} &= \check{\mathbf{P}}_{k+1} \mathbf{H}_{k+1}^\top \left(\mathbf{H}_{k+1} \check{\mathbf{P}}_{k+1} \mathbf{H}_{k+1}^\top + \mathbf{R}_{k+1} \right)^{-1}, \\ \hat{\mathbf{P}}_{k+1} &= (\mathbf{1} - \mathbf{K}_{k+1} \mathbf{H}_{k+1}) \check{\mathbf{P}}_{k+1}, \\ \delta \hat{\mathbf{x}}_{k+1} &= \mathbf{K}_{k+1} \bar{\epsilon}_{k+1}. \end{aligned} \quad (20)$$

The state \mathbf{x} is updated using the perturbation $\delta \hat{\mathbf{x}}_{k+1}$.

3) *Composition Step*: The robocentric model requires state set values referencing \mathcal{F}_{r_k} to be the robot reference frame associated with the latest camera measurement. After performing the EKF measurement update, the inertial and robot states are updated from \mathcal{F}_{r_k} to $\mathcal{F}_{r_{k+1}}$ using the composition step:

$$\begin{aligned} \hat{\mathbf{C}}_{r_{k+1}i} &= \hat{\mathbf{C}}_{r_k v_{k+1}}^\top \hat{\mathbf{C}}_{r_k i}, \quad \hat{\mathbf{g}}_{r_{k+1}} = \hat{\mathbf{C}}_{r_k v_{k+1}}^\top \hat{\mathbf{g}}_{r_k}, \\ \hat{\mathbf{r}}_{r_{k+1}}^{i r_{k+1}} &= \check{\mathbf{C}}_{r_k v_{k+1}}^\top \left(\hat{\mathbf{r}}_{r_k}^{i r_k} - \hat{\mathbf{r}}_{r_k}^{v_{k+1} r_k} \right), \\ \check{\mathbf{C}}_{r_{k+1} v_{k+1}} &= \mathbf{1}, \quad \check{\mathbf{r}}_{r_{k+1}}^{i r_{k+1}} = \mathbf{0}. \end{aligned} \quad (21)$$

The state covariance is accordingly updated using

$$\hat{\mathbf{P}}_{k+1} = \mathbf{U}_{k+1} \hat{\mathbf{P}}_{k+1} \mathbf{U}_{k+1}^\top, \quad \mathbf{U}_{k+1} = \frac{\partial \delta \hat{\mathbf{x}}_{k+1}}{\partial \delta \hat{\mathbf{x}}_{k+1}}. \quad (22)$$

The derivation and value of \mathbf{U}_{k+1} can be found in [12].

D. End-to-End Training with the Differentiable EKF

Figure 2 visualizes the training procedure of our hybrid system. We extend the amount of frames per sample from the standard of three (i.e., one target image, and two adjacent source images) to an arbitrary length N . The longer sequence length is important for uncertainty learning because the network must learn to inflate the covariance for erroneous measurements that negatively impact future state estimates. By reducing the impact of erroneous measurements, future estimates will be more accurate, and the reconstruction loss at these timesteps will be reduced.

The EKF propagates from the initial pose \mathbf{x}_0 , and incorporates the learned egomotion measurements. Then, the *a posteriori* robot pose is used to compute the minimum reconstruction loss (Equation (3)). This loss requires two image reconstructions. The first uses the “forward” egomotion predictions to produce $\mathbf{I}_{t-1 \rightarrow t}$. The second uses the “inverse” predictions (i.e the source-target image inputs are swapped) to produce $\mathbf{I}_{t+1 \rightarrow t}$.

1) *Pose Initialization Scheme*: During training, each training sample must be initialized with an accurate estimate of the state (and state covariance) at the initial timestep. With supervised training, this step is trivial: the filter is initialized with the initial pose ground truth. Since ground truth information is not available in the self-supervised loss formulation, initialization is more complicated. Instead of using ground truth, we initialize the training samples using the most recent pose estimate from our hybrid VIO system. The pose estimates for all training sequence frames are generated at the start of every epoch, and remain fixed in each epoch. As training progresses, the pose estimate improves, so the initialization accuracy increases. The increase in initialization accuracy allows the training to converge further.

To ensure a reasonable initialization for the first epoch, pose estimates are generated using a pretrained *unscaled* egomotion network, which we trained using the self-supervised losses from Section III-B. To enable a metrically scaled pose initialization, a scale parameter λ is augmented to the end of the state (similar to [27]). The continuous time dynamics model for the scale is $\dot{\lambda} = 0$, and error state is $\delta\lambda = 0$. Within the measurement model, λ is used to align the translation scales in ϵ_r through $\tilde{\mathbf{r}}_{c_k}^{c_{k+1}c_k} - \lambda \mathbf{r}_{c_k}^{c_{k+1}c_k}$. The rotation measurement is unchanged. The measurement Jacobian becomes:

$$\mathbf{H}_{k+1} = \begin{bmatrix} \mathbf{0}_{9 \times 3} & -\mathbf{C}_{rc}^T \mathbf{J}_\ell(-\tilde{\phi}) & \mathbf{0}_{3 \times 3} & \mathbf{0}_{9 \times 3} & \mathbf{0}_{1 \times 3} \\ \mathbf{0}_{9 \times 3} & \mathbf{C}_{rc}^T \tilde{\mathbf{C}}_r^{cr\wedge} & -\mathbf{C}_{rc}^T \lambda & \mathbf{0}_{9 \times 3} & -\mathbf{C}_{rc}^T \tilde{\mathbf{r}} \end{bmatrix}, \quad (23)$$

where the subscripts for the state are removed for brevity.

Initializing \mathbf{x}_0 with metric scale in the training process allows the depth and egomotion prediction scales to converge to unity. Figure 3 demonstrates the scale-aware translation predictions from the trained egomotion network. At test time, scale no longer needs to be estimated, but can be utilized if the test-time environment changes dramatically.

2) *Uncertainty-Aware Measurement Model*: To leverage the learned egomotion measurements within the filter, the iterative egomotion network [26] estimates a measurement covariance $\mathbf{R}_k = \begin{bmatrix} \Sigma_{\phi_k} & \mathbf{0}_{3 \times 3} \\ \mathbf{0}_{3 \times 3} & \Sigma_{r_k} \end{bmatrix}$, where Σ_{r_k} and Σ_{ϕ_k} are diagonal covariance matrices. Similar to [8], the network’s final layer dimensionality is increased from 6 to 12. The additional 6 outputs w_i populate the diagonal of \mathbf{R}_k through $\sigma_i^2 = \sigma_0^2 10^{\beta \tanh(w_i)}$, where σ_0^2 is a base covariance, and $\beta \in \mathbb{R}_{>0}$ is a control parameter.

Similar to the iterative update of the initial egomotion network predictions through multiple forward passes, the uncertainty predictions are iteratively refined. Additional

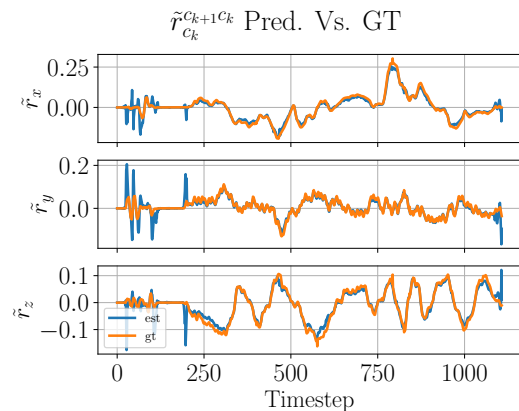


Fig. 3: The raw translation predictions for EuRoC validation sequence MH05. The scale of the predictions closely matches that of the ground truth, indicating that the networks are scale-aware.

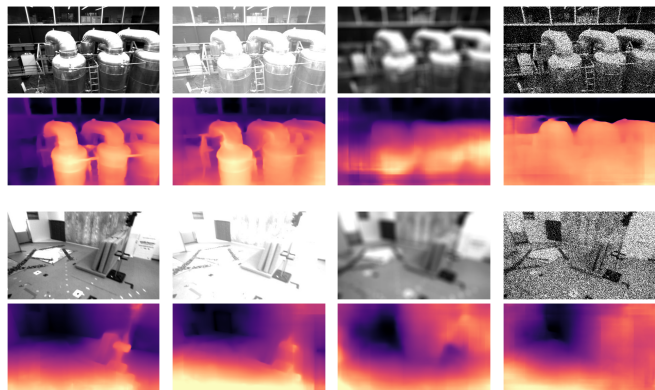


Fig. 4: Images from the EuRoC dataset validation sequences, and the resulting image after our applied brightness, blur, and shot noise corruptions. Despite severe image degradation, the depth network reasonably estimates the scene depth.

forward passes improve the alignment of the input images, which enables the network to observe discrepancies between images. These discrepancies indicate prediction errors, so the network learns to inflate the covariance prediction in sequences with high discrepancy levels.

IV. EXPERIMENTS & RESULTS

We trained and evaluated our system on the EuRoC dataset [28], which contains visual-inertial data collected on-board an AscTec Firefly Micro Aerial Vehicle (MAV). This dataset consists of 11 sequences that are collected within three different environments. The vehicle is manually operated throughout these sequences and undergoes rapid movement that produces motion blur in the image stream, making this dataset challenging for odometry estimation. The MAV is equipped with a global shutter stereo camera operating at 20 Hz and a Skybotix IMU sensor operating at 200 Hz. The visual-inertial measurements are synchronized on-board, and the extrinsic/intrinsic calibration parameters are provided. Although ground truth is available, these data are only used to evaluate our self-supervised approach. In our experiments, the images were undistorted using the provided

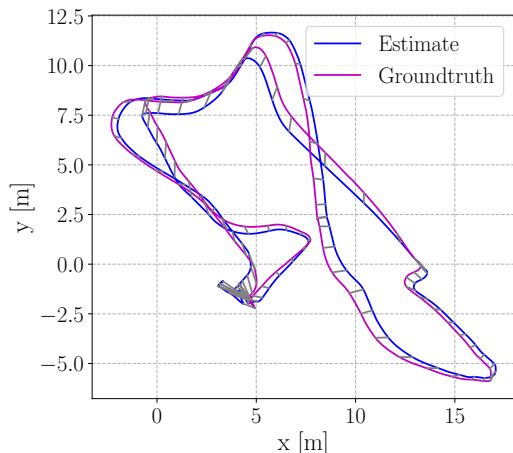


Fig. 5: Topdown trajectory estimate for EuRoC sequence MH05 after Sim3 alignment.

radial-tangential parameters and downsized to 256×448 . The left and right images from all sequences except MH05, V103, and V203 were used during training. The left and right images were treated as independent sequences because our method is purely monocular at training and inference time.

A. Training Details

Our system was trained in PyTorch [29] using an Nvidia Quadro RTX 8000 GPU. We used the depth and egomotion networks from [26]. Initially, the model was pretrained on the ScanNet dataset, and then refined on the EuRoC training sequences. The EuRoC IMU and image data used to train our system were downsampled by a factor of two to reduce the per-epoch training time and increase the perspective change between frames. The training samples consisted of subsequences that were 1 second (10 images at 10 Hz) in length. Adjacent training samples had an overlap of 0.3 s. The depth and egomotion networks were trained, in mini-batches of six samples, via gradient descent (using the Adam optimizer [30] with $\beta_1 = 0.9$, $\beta_2 = 0.999$) for 25 epochs with a learning rate of $1e^{-4}$ that was halved every seven epochs. Five egomotion iterations (i.e., forward passes) were applied at training and test time. For image augmentation during training, we randomly applied brightness, contrast, saturation, and hue transformations, in addition to random horizontal flips ($p = 0.5$); the same augmentation was applied to every image within the same training sample.¹ For our training losses, we set $\alpha = 0.15$, and the weights for the various losses were $\lambda_{photo} = 1$, $\lambda_{smooth} = 0.05$, and $\lambda_{consist} = 0.15$. The constants for uncertainty prediction were $\beta = 4$ and $\sigma_0^2 = 1$. Our IMU noise parameters were $\sigma_\omega = 1e^{-3}$, $\sigma_a = 0.1$, $\sigma_{b_\omega} = 1e^{-5}$, $\sigma_{b_a} = 0.01$, and the covariance initialization \mathbf{P}_0 used during training consisted of $\sigma_{g_0} = 0.1$, $\sigma_{v_0} = 0.01$, $\sigma_{b_{a_0}} = 1$, $\sigma_{b_{\omega_0}} = 0.1$.

¹Since the IMU data cannot be augmented in a similar manner, the egomotion predictions, prior to use within the EKF, were appropriately altered to represent the egomotion of the unflipped image.

TABLE I: Translation RMSE for the EuRoC sequences (using the ROVIO and VINS-Mono results reported in [31]). Our self-supervised system outperforms the supervised variant by a significant margin.

Sequence	ROVIO [11]	VINS-Mono [13]	Self-VIO [5]	EKF-VIO [8]	Ours
MH01	0.21	0.27	0.19	1.17	0.51
MH02	0.25	0.12	0.15	1.56	0.78
MH03	0.25	0.13	0.21	1.89	0.69
MH04	0.49	0.23	0.16	2.12	1.00
MH05 [†]	0.52	0.35	0.29	1.96	0.80
V101	0.10	0.07	0.08	2.07	0.43
V102	0.10	0.10	0.09	2.20	0.61
V103 [†]	0.14	0.13	0.10	2.83	0.72
V201	0.12	0.08	0.11	1.49	0.20
V202	0.14	0.08	0.08	2.22	0.81
V203 [†]	0.14	0.21	0.11	—	0.84

[†] These sequences are within the held-out validation set.

B. EuRoC Dataset Results

Table I reports the average translation RMSE, after Sim3 alignment, for various VIO algorithms operating on the EuRoC sequences. Similar to other self-supervised methods [5], we report the training sequence results. We include comparisons with classical systems (ROVIO and VINS-Mono), learning-based systems (Self-VIO), and hybrid systems (the differentiable EKF approach from Li et al. [8]). Notably, our system is significantly more accurate than the (supervised) hybrid approach from [8], but Self-VIO outperforms our system. We attribute this result to the adversarial loss in Self-VIO, which led to more accurate depth predictions. However, Self-VIO cannot produce metrically scaled predictions, and relies on Sim3 alignment to recover scale. Figure 5 visualizes our system’s accuracy on MH05.

C. Visual Degradation Experiment

Next, we investigate how robust our hybrid method is to a number of realistic visual degradations. For this experiment, our VIO approach and other VIO approaches were tested on EuRoC validation sequences that had degraded image streams. Section IV-C.1 and Section IV-C.2 describe the image stream degradations, while Section IV-C.3 presents our experimental results.

1) *Image Corruptions*: The images were corrupted in three ways: applied brightness transformations, applied defocus blurring, and added shot noise. The corruptions were applied using the ImgAug library², and a severity level of five was chosen. Only one corruption at a time was applied. Figure 4 shows various corrupted EuRoC images. For our experiments, we applied each corruption to all images within a window of 20s, every 40s (i.e., half the images were corrupted).

2) *Frame Skipping*: To simulate a larger perspective change, or a reduced camera/IMU framerate, we downsampled the image and IMU frequency across the full validation sequences. In our notation, $1:X$ refers a downsample rate of X , where only one of X frames is maintained (e.g., $1:2$ removes half of the frames). We tested downsample rates of $X \in \{2, 3, 4\}$.

²See <https://imgaug.readthedocs.io/en/latest/>

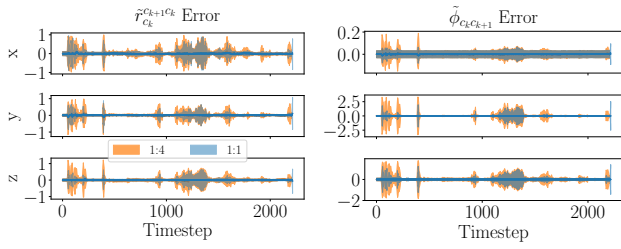


Fig. 6: The learned relative egomotion measurement errors with their associated 1σ uncertainty bound for the full sequence (1:1), and quarter-frame sequence (1:4). The learned measurement covariance naturally inflates for the 1:4 sequence due to the larger perspective change between frames.

3) *Degradation Experiment Results:* We evaluated our system, along with several others, on this visually degraded data. Namely, for classical estimators, we tested VINS-Mono [13], ROVIO [11], and R-VIO [12], and for a learning-based system, we evaluated the tightly-coupled (vision-only) system [26] (note that SelfVIO [5] was not publicly available).³ Table II depicts the experimental results for sequences MH05 and V103. We observe that degraded conditions caused the classical estimators to fail in a significant number of trials. During these failures, the classical estimators either stopped (e.g., due to lost feature tracking) or diverged (resulting in 100+ meters of error). The most robust classical system was VINS-Mono, but it could not maintain feature tracking in the frame skip experiments. On the other hand, our robust system performed consistently in most trials. Notably, the extreme 1:4 case caused little to no increase in error for our robust system. Figure 6 is a plot of the network’s measurement error and the predicted covariance for the 1:1 and 1:4 cases. The covariance predictions, in Figure 6, inflate when the network experiences extreme motion.

D. Ablation Study

Figure 7 shows the relative translation and rotation errors when the iterative egomotion network, and the EKF component are removed at training and test time. From Figure 7, it is apparent that integrating the gyroscope measurements in the EKF is crucial for accurate orientation estimates. The iterative egomotion network, when paired with the EKF, reduces the overall translation error.

Table III depicts the mean accuracy for three versions of our system in the corrupted sequences from Table II. The first is our proposed hybrid system. The second is the egomotion network from our system, evaluated with the EKF removed (i.e., the EKF was present during training, but removed at test time). The third is the same egomotion network trained without the EKF (i.e., the baseline system from [26]). Notably, the presence of the EKF during training improves the accuracy of the network measurements.

³For these comparisons, we used the open source implementations, with their default EuRoC parameters, ran on Ubuntu 20.04 with ROS Noetic.

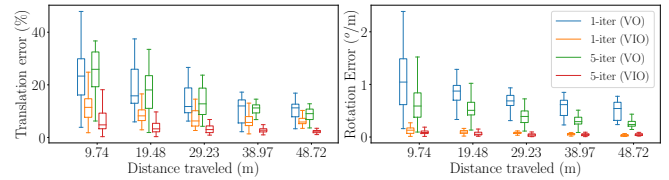


Fig. 7: Ablation study showing the effect of the iterative egomotion network, and the addition of the EKF for sequence MH05.

V. CONCLUSION

We have demonstrated how a self-supervised, hybrid VIO system is able to effectively maintain an estimate of a robot’s state, despite operating within significantly degraded visual environments. Our system, which can be trained end-to-end with a self-supervised reconstruction loss, is able to learn a heteroscedastic measurement covariance model that down-weights unreliable egomotion measurements. Combined with an IMU-based process model in a differentiable EKF, our principled sensor fusion scheme increases the overall accuracy of our system and allows for consistent performance within visually degraded environments. A noteworthy attribute of our monocular system is its ability to naturally recover metric scale.

Future work involves improving the depth predictions to boost the accuracy of the iterative egomotion network. We plan to do so by incorporating the discriminative loss from [5], and investigating how raw depth predictions can be refined with a differentiable filter. Additionally, we plan to investigate the possibility of self-calibration with our system.

ACKNOWLEDGMENTS

We gratefully acknowledge the contribution of NVIDIA Corporation, who provided the Quadro RTX 8000 GPU used for this research.

REFERENCES

- [1] J. Gui, D. Gu, S. Wang, and H. Hu, “A review of visual inertial odometry from filtering and optimisation perspectives,” *Adv. Robot.*, vol. 29, no. 20, pp. 1289–1301, 2015.
- [2] M. Gurturk, A. Yusefi, M. Aslan, M. Soyacan, A. Durdu, and A. Masiero, “The YTU dataset and recurrent neural network based visual-inertial odometry,” *Measurement*, vol. 184, p. 109878, 2021.
- [3] C. Chen, S. Rosa, Y. Miao, C. Lu, W. Wu, A. Markham, and N. Trigoni, “Selective sensor fusion for neural visual-inertial odometry,” in *Proc. IEEE Conf. Comput. Vision Pattern Recognition (CVPR)*, 2019, pp. 10 542–10 551.
- [4] R. Clark, S. Wang, H. Wen, A. Markham, and N. Trigoni, “Vinet: Visual-inertial odometry as a sequence-to-sequence learning problem,” in *Proc. AAAI Conf. on Artificial Intell.*, vol. 31, no. 1, 2017.
- [5] Y. Almalioglu, M. Turan, A. Sari, M. Saputra, P. de Gusmão, A. Markham, and N. N. Trigoni, “SelfVIO: Self-supervised deep monocular visual-inertial odometry and depth estimation,” *arXiv preprint arXiv:1911.09968*, 2019.
- [6] P. Wei, G. Hua, W. Huang, F. Meng, and H. Liu, “Unsupervised monocular visual-inertial odometry network,” in *Proc. Int. Joint Conf. Artificial Intell. (IJCAI)*, 2021, pp. 2347–2354.
- [7] A. Kloss, G. Martius, and J. Bohg, “How to train your differentiable filter,” *Autonomous Robots*, vol. 45, no. 4, pp. 561–578, 2021.
- [8] C. Li and S. Waslander, “Towards end-to-end learning of visual inertial odometry with an EKF,” in *Proc. Conf. Computer Robot Vision (CRV)*. IEEE, 2020, pp. 190–197.
- [9] A. Mourikis and R. S., “A Multi-State Constraint Kalman Filter for Vision-aided Inertial Navigation,” in *Proc. IEEE Int. Conf. Robot. Autom. (ICRA)*, vol. 2, 2007, p. 6.

TABLE II: Results for the degraded EuRoC validation sequences. We considered a failure when 1) feature tracking was lost, or 2) the optimization diverged, resulting in rapid error growth on the order of 100+ m. Failures are indicated with an x. Despite not encountering these degradations during training, our hybrid approach maintains its accuracy.

Corruption Type	Trans. RMSE (Sim3)					Rot. RMSE (Sim3)				
	Ours	Learned VO [26]	VINS-Mono	ROVIO	R-VIO	Ours	Learned VO [26]	VINS-Mono	ROVIO	R-VIO
MH05 Nominal	0.93	4.04	0.28	1.01	0.46	3.57	11.35	12.95	4.09	2.36
Brightness	1.11	4.16	0.29	1.64	x	6.32	14.56	15.32	4.38	x
Blur	1.48	3.85	0.38	1.20	0.48	5.56	36.06	13.18	3.47	1.68
Shot	2.07	4.70	0.63	1.54	0.99	12.66	46.77	14.08	5.55	4.54
(1:2) Nominal	0.70	2.74	0.27	x	x	4.77	9.17	16.28	x	x
Brightness	1.09	2.72	0.34	x	x	7.17	12.69	16.52	x	x
Blur	1.71	3.92	0.71	x	x	6.95	35.96	17.41	x	x
Shot	2.43	4.15	0.67	x	x	10.93	34.60	14.20	x	x
(1:3) Nominal	0.69	2.18	0.62	x	x	4.26	9.41	17.14	x	x
(1:4) Nominal	0.67	1.93	0.41	x	x	6.08	10.66	15.65	x	x
V103 Nominal	0.43	0.94	0.15	0.21	0.21	9.79	15.86	5.92	2.70	6.89
Brightness	0.53	0.92	0.17	0.21	x	9.09	14.17	6.25	3.88	x
Blur	0.82	0.81	0.25	0.26	x	17.35	33.19	5.71	4.61	x
Shot	0.59	1.33	0.50	0.23	x	15.12	124.24	9.50	3.55	x
(1:2) Nominal	0.72	0.72	x	x	x	15.07	15.52	x	x	x
Brightness	0.86	0.70	x	x	x	15.56	16.19	x	x	x
Blur	0.91	0.62	x	x	x	24.64	30.70	x	x	x
Shot	0.84	1.26	x	x	x	16.57	64.03	x	x	x
(1:3) Nominal	0.73	0.68	x	0.73	x	15.77	17.38	x	8.94	x
(1:4) Nominal	1.02	0.88	x	x	x	20.13	36.07	x	x	x
# Failures	0	0	6	11	15	0	0	6	11	15
Avg.	1.02	2.16	—	—	—	11.37	29.43	—	—	—

TABLE III: The mean error for three variations of our approach in the (corrupted) Table II sequences. With the vision-only approaches, the network trained with our hybrid system is more accurate than the same network trained without the EKF.

Trans. RMSE			Rot. RMSE		
Ours	Ours (w/o EKF)	Learned VO [26]	Ours	Ours (w/o EKF)	Learned VO [26]
1.02	1.52	2.16	11.37	17.09	29.43

- [10] M. Li and A. Mourikis, “High-precision, consistent EKF-based visual-inertial odometry,” *Int. J. Robot. Res. (IJRR)*, vol. 32, no. 6, pp. 690–711, 2013.
- [11] M. Bloesch, M. Burri, S. Omari, M. Hutter, and R. Siegwart, “Iterated extended Kalman filter based visual-inertial odometry using direct photometric feedback,” *Int. J. Robot. Res. (IJRR)*, vol. 36, no. 10, pp. 1053–1072, 2017.
- [12] Z. Huai and G. Huang, “Robocentric visual-inertial odometry,” in *Proc. Conf. IEEE/RSJ Int. Conf. Intell. Robot. Syst. (IROS)*. IEEE, 2018, pp. 6319–6326.
- [13] T. Qin, P. Li, and S. Shen, “Vins-mono: A robust and versatile monocular visual-inertial state estimator,” *IEEE Trans. Robot.*, vol. 34, no. 4, pp. 1004–1020, 2018.
- [14] S. Leutenegger, S. Lynen, M. Bosse, R. Siegwart, and P. Furgale, “Keyframe-based visual-inertial odometry using nonlinear optimization,” *Int. J. Robot. Res. (IJRR)*, vol. 34, no. 3, pp. 314–334, 2015.
- [15] C. Forster, L. Carlone, F. Dellaert, and D. Scaramuzza, “IMU preintegration on manifold for efficient visual-inertial Maximum-a-Posteriori Estimation,” in *Proc. Robotics: Science and Systems (RSS)*, 2015.
- [16] T. Zhou, M. Brown, N. Snavely, and D. Lowe, “Unsupervised Learning of Depth and Ego-Motion from Video,” in *Proc. IEEE Conf. Comput. Vision Pattern Recognition (CVPR)*, 2017, pp. 1851–1858.
- [17] T. Haarnoja, A. Ajay, S. Levine, and P. Abbeel, “Backprop KF: Learning discriminative deterministic state estimators,” in *Proc. Conf. Neural Inf. Process. Syst. (NeurIPS)*, 2016, pp. 4376–4384.
- [18] L. Zhou, Z. Luo, T. Shen, J. Zhang, M. Zhen, Y. Yao, T. Fang, and L. Quan, “Kfnet: Learning temporal camera relocalization using kalman filtering,” in *Proc. IEEE/CVF Conf. Comput. Vision Pattern Recognition (CVPR)*, 2020, pp. 4919–4928.
- [19] Z. Chen, H. Du, Y. Liao, Y. Wang, and R. Xiong, “Fully differentiable and interpretable model for VIO with 4 trainable parameters,” *arXiv preprint arXiv:2109.12292*, 2021.
- [20] C. Chen, C. Lu, B. Wang, N. Trigoni, and A. Markham, “DynaNet: Neural Kalman dynamical model for motion estimation and prediction,” *IEEE Trans. Neural Networks Learning Syst.*, vol. 32, no. 12, pp. 5479–5491, 2021.
- [21] M. Jaderberg, K. Simonyan, A. Zisserman, and K. Kavukcuoglu, “Spatial Transformer Networks,” in *Proc. Conf. Neural Inf. Process. Syst. (NeurIPS)*, 2015, pp. 2017–2025.
- [22] Z. Wang, A. Bovik, H. Sheikh, and E. Simoncelli, “Image quality assessment: from error visibility to structural similarity,” *IEEE Trans. Image Process.*, vol. 13, no. 4, pp. 600–612, 2004.
- [23] C. Godard, O. Aodha, M. Firman, and G. Brostow, “Digging into self-supervised monocular depth estimation,” in *IEEE Conf. Comput. Vision Pattern Recognition (CVPR)*, 2019, pp. 3828–3838.
- [24] C. Godard, O. Aodha, and G. Brostow, “Unsupervised monocular depth estimation with left-right consistency,” in *Proc. IEEE Conf. Comput. Vision Pattern Recognition (CVPR)*, 2017, pp. 270–279.
- [25] J. Bian, Z. Li, N. Wang, H. Zhan, C. Shen, M. Cheng, and I. Reid, “Unsupervised scale-consistent depth and ego-motion learning from monocular video,” in *Proc. Conf. Neural Inf. Process. Syst. (NeurIPS)*, 2019, pp. 35–45.
- [26] B. Wagstaff, V. Peretroukhin, and J. Kelly, “Self-Supervised Structure-from-Motion through Tightly-Coupled Depth and Egomotion Networks,” *arXiv preprint arXiv:2106.04007*, 2021.
- [27] C. Li, “Towards End-to-End Learning of Monocular Visual-Inertial Odometry with an Extended Kalman Filter,” Ph.D. dissertation, University of Toronto (Canada), 2020.
- [28] M. Burri, J. Nikolic, P. Gohl, T. Schneider, J. Rehder, S. Omari, M. Achtelik, and R. Siegwart, “The EuRoC micro aerial vehicle datasets,” *Int. J. Robot. Res. (IJRR)*, vol. 35, no. 10, pp. 1157–1163, 2016.
- [29] A. Paszke, S. Gross, S. Chintala, G. Chanan, E. Yang, Z. DeVito, Z. Lin, A. Desmaison, L. Antiga, and A. Lerer, “Automatic Differentiation in PyTorch,” in *Workshop on Automatic Differentiation, Conf. Neural Inf. Process. Syst. (NeurIPS)*, 2017.
- [30] D. P. Kingma and J. Ba, “Adam: A Method for Stochastic Optimization,” *arXiv preprint arXiv:1412.6980*, 2014.
- [31] J. Delmerico and D. Scaramuzza, “A benchmark comparison of monocular visual-inertial odometry algorithms for flying robots,” in *Proc. IEEE Int. Conf. Robot. Autom. (ICRA)*. IEEE, 2018, pp. 2502–2509.